Fiber-based confocal microscope for cryogenic spectroscopy

Alexander Högele,[1,a)] Stefan Seidl,[1] Martin Kroner,[1] Khaled Karrai,[1]
Christian Schulhauser,[2] Omar Sqalli,[2,b)] Jan Scrimgeour,[3] and Richard J. Warburton[3]

[1]*Center for NanoScience, Department für Physik, Ludwig-Maximilians-Universität,
Geschwister-Scholl-Platz 1, 80539 München, Germany*
[2]*Attocube Systems AG, Königinstr 11a, 80539 München, Germany*
[3]*School of Engineering and Physical Sciences, Heriot-Watt University, Edinburgh EH14 4AS,
United Kingdom*

We describe the design and performance of a fiber-based confocal microscope for cryogenic operation. The microscope combines positioning at low temperatures along three space coordinates of millimeter translation and nanometer precision with high stability and optical performance at the diffraction limit. It was successfully tested under ambient conditions as well as at liquid nitrogen (77 K) and liquid helium (4 K) temperatures. The compact nonmagnetic design provides for long term position stability against helium refilling transfers, temperature sweeps, as well as magnetic field variation between −9 and 9 T. As a demonstration of the microscope performance, applications in the spectroscopy of single semiconductor quantum dots are presented. © *2008 American Institute of Physics.* [DOI: 10.1063/1.2885681]

I. INTRODUCTION

Optical spectroscopy of single nano-objects such as self-assembled semiconductor quantum dots, color centers in diamond, and semiconductor nanocrystals places many challenging demands on the optical system. The simplest optical system is a confocal microscope: provided that the density of nano-objects is low enough, single nano-objects can be probed with negligible cross-talk from neighboring nano-objects with high throughput efficiency and with very high control of the optical polarization. Exploiting the high optical and spin coherence of quantum dots typically involves working at low temperatures of liquid helium. Designing a confocal microscope for low temperature operation is challenging. Ideally, the objective should have a high numerical aperture (NA) operating at the diffraction limit and sample scanning should be possible with nm precision over a mm range even at low temperature. Furthermore, contemporary studies involve probing the properties of a single nanostructure in a large parameter space defined by applied electric and magnetic fields, temperature, optical pump power, and possibly also microwave fields. This means that it is highly desirable to have a drift-free system so that continuous realignment of the microscope is not required, when sweeping a magnetic field, changing the temperature or even refilling the cryostat. One possible design employs an optical window cryostat which are widely used for macroscopic and microscopic spectroscopies. The use of optical bath cryostats commonly requires expensive long-distance high-resolution objectives to probe microscopic and nanoscopic objects and the large separation between sample and objective results in

stability and drift problems. A more compact system can be constructed using small continuous flow cryostats but these tend to introduce vibrations and, in our experience, drift of the focus relative to the sample remains a problem. In both these approaches, a long term position stability of the sample inside the cryostat with respect to the room-temperature optics is restricted owing to the large temperature gradient. The stability requirement is in fact a particularly stringent requirement for single nano-object spectroscopy: the focal spot should move by no more than a few 100 nm over the course of a long experiment. This condition is relaxed in ensemble spectroscopy when a large amount of signal averaging is performed and implies that in many cases, setups for ensemble measurements are inappropriate for single nano-object spectroscopy.

In this article, we describe a fiber-based optical microscope for cryogenic operation which combines precise and reliable sample scanning, high mechanical stability with negligible drift over many days of operation involving temperature and magnetic field sweeps and diffraction-limited optical performance. We describe the mechanical and optical design and present results of test experiments. As a demonstration of the high performance of our home-built system, we present photoluminescence (PL) and magnetophotoluminescence from −9 to 9 T on single semiconductor based self-assembled InGaAs quantum dots (QDs) at liquid helium temperatures. The microscope is clearly appropriate for spectroscopy of other nano-objects and in fact can be used not only at low temperatures but in other harsh environments, for instance, ultrahigh vacuum.

II. FIBER-BASED MICROSCOPE FOR CRYOGENIC SPECTROSCOPY

In order to comply with the condition of stable, drift-free excitation, and collection of the optical response, it is essential to fix the relative position of the sample, the objective,

---

a)Author to whom correspondence should be addressed. Present address: Institute of Quantum Electronics, ETH Hönggerberg HPT G14.2, CH-8093 Zürich, Switzerland. Electronic mail: hoegele@phys.ethz.ch.
b)Present address: SHG Technovation, Via Cantonale 35a, CH-6928 Manno-Lugano, Switzerland.
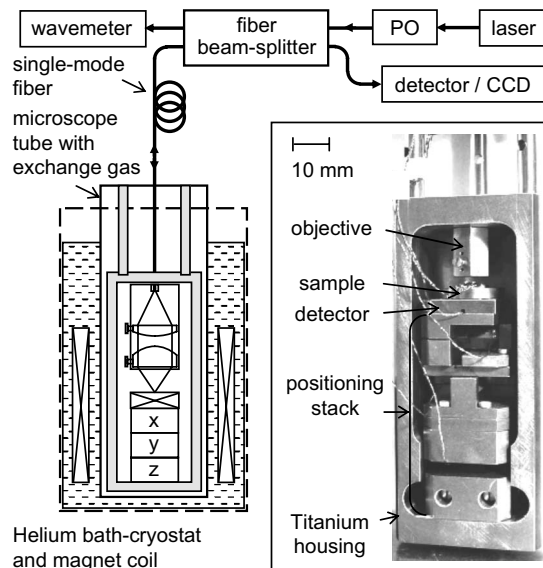
© 2008 American Institute of Physics

FIG. 1. Setup schematics (not to scale): the excitation light of a tunable laser is coupled into the fiber beam splitter after passing through polarizing optical components. The laser wavelength is monitored through one output arm of the beam splitter with a wavemeter. The other output is connected to the single-mode microscope fiber. The fiber delivers the excitation light to the sample mounted on a low-temperature xyz-positioning unit. The sample is positioned in the focal plane of the two-lens microscope. The microscope is mounted in a tube containing helium exchange gas which allows thermal equilibrium with the helium bath cryostat (dashed box) at 4.2 K to be established. A superconducting coil provides magnetic fields from −9 to 9 T. A silicon photodetector is sandwiched between the sample and the positioning unit for the detection of the optical transmission. The reflected signal as well as the backscattered response of the sample retraces its path through the fiber to the beam splitter where it is diverted to a silicon detector for power analysis or, alternatively, to a monochromator with a nitrogen cooled CCD for spectrometry. Inset: microscope components inside the titanium housing in more detail.

and the ocular. In a case where the relative displacement by mechanical deformation due to thermal or magnetic gradients cannot be ruled out, a close spacing between the sample and the objective lens as well as the objective lens and the ocular is desirable in order to minimize the optical lever arm. As a consequence, our concept is based on a miniaturization of an optical two-lens system placed together with the sample and its positioning unit in a monolithic housing, as shown in Fig. 1. A glass fiber serves as an optical guide for both the excitation and the response from the sample. The fiber provides the connection between the harsh environment, in our case, low temperature, and the rest of the experiment. Furthermore, by using a single-mode fiber, we ensure confocal detection, the single-mode fiber playing the same role as the pinhole[1] in a conventional confocal microscope.[2]

A. Mechanical design and positioning

Low temperature operation in conventional liquid helium bath cryostats places a restriction on the overall size of the microscope, particularly for measurements in magnetic field. Our commercial cryostat (CryoVac, 22 l) contains a superconducting solenoid magnet (Oxford Instruments) with an inner cross section of 50.8 mm (2 in.) limiting the outer diameter of the microscope housing. Furthermore, the plane

of maximum magnetic field is located in the center of the magnet coil, ~1.0 m below the top flange of the cryostat (Fig. 1). This is quite standard: clearly, it is necessary to place the magnet adjacent to the bottom of the cryostat in order to provide the best cooling of the superconducting coil.

Since our microscope concept implies that both objective and ocular lenses are placed inside the cryostat, vertical positioning of the sample into the focal plane as well as lateral translation are necessarily carried out at low temperatures. A well known fact is that lubricant-based positioning systems are not compatible with low temperature but dynamic piezoelectric sliders can provide lateral[3] and vertical[4] translations. We use a piezobased xyz-positioning unit which is also available as a commercial version (attocube systems, ANP-100). It combines high translation distance of ~7.5 mm/axis with high positioning precision (down to ~5 nm in the slip-stick mode and angstrom-scale in the constant voltage mode at 4.2 K). Titanium was used as a nonmagnetic material for the fabrication of the positioners, the housing of the microscope and the two-lens optical system as well as detector mounts (Fig. 1, inset).

B. Optical design

The optical design of the microscope objective is rather simple: two aspheric lenses, a collimating lens (Geltech Aspheric Collimator Lens 350430, $f=5.0$ mm, clear aperture of 1.50 mm) with NA of 0.15 and a focusing lens (Geltech Aspheric Collimator Lens 350140, $f=1.45$ mm, clear aperture of 1.60 mm) with NA=0.55 form the confocal arrangement where the core (5.8 μm mode-field diameter at 950 nm wavelength) of the single-mode fiber acts as a pinhole. For the focusing lens, high NA is desirable for high resolution and collection efficiency. The boundary conditions for the choice of the collimating lens were, first, to match the NA to that of the optical fiber (0.13) and, second, to match the clear aperture to that of the objective. The slight mismatch in NAs of the fiber and the collimating lens yields an effective clear aperture of 1.3 mm which in turn results in an effective NA of our objective of 0.45. The lenses were glued in titanium housings. The collimator was fixed in position relative to the optical fiber using a grub screw by collimating a beam at the relevant wavelength, in our case 950 nm. The objective was then placed in the microscope housing. The choice of aspheric lenses means that there is close to zero spherical aberration on-axis. This feature is exploited in imaging applications by scanning the sample. This is clearly a very attractive feature. However, the two aspheric lenses inevitably suffer from chromatic aberrations, as shown in Fig. 2. For a range of wavelengths (500–1100 nm as confirmed experimentally), good performance is possible by adjusting the z-position of the sample. Problems arise when more than one wavelength are involved, for instance, in a PL experiment. The chromatic aberrations are minimized in the design by using very small lenses, just millimeter in diameter.

For cryogenic operation, the microscope was placed in a stainless steel tube and evacuated to a pressure below 10^{-4} mbar. Helium exchange gas was fed into the tube up to a pressure of 20–30 mbar in order to provide a thermal con-
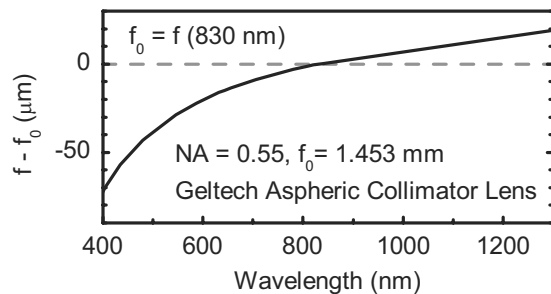
FIG. 2. Calculated focal plane displacement as a function of illumination wavelength (Geltech aspheric lens No. 350140, Corning glass C0550). The reference focal length for 830 nm wavelength illumination of the aspheric collimator lens with the numerical aperture NA=0.55 is f_0=1.453 mm.

tact to the liquid helium inside the bath cryostat. Insertion of a fiber beam splitter provided a convenient way to access light reflected from the microscope (Fig. 1).

III. MICROSCOPE SPECIFICATIONS AND PERFORMANCE

A. Focal plane and Fabry–Pérot characteristics

In order to gauge the axial position of the focal plane, one relies on the change in transmitted and reflected powers as the sample is moved through the focus of the objective. Figure 3(a) shows how the reflected power undergoes two pronounced resonances as the sample is moved upward. The first resonance A corresponds to the reflection at the GaAs heterostructure surface, and the second, labeled B, reflection at the sample backside. The ratio of the two peaks is A/B ~4 as expected from the amplitude reflection coefficients determined by the difference in the refractive indices of the vacuum n_{vac} and the sample n_2.

For the optical transmission and reflectivity characteristics, there is an additional reflecting interface between the vacuum and the polished fiber end and the refractive index of glass n_1 has to be taken into account. In fact, the two interfaces, namely, the fiber-vacuum and the vacuum-sample interface, along with the two aspheric lenses form a confocal Fabry–Pérot resonator with a characteristic length D, albeit with low finesse. Figure 3(c) shows the normalized transmission and reflectivity of the optical cavity fitted to the Fabry–Pérot functions $\mathcal{T}=1/(1+F \sin^2 \Phi)$ and $\mathcal{R}=1-\mathcal{T}$, respectively. The phase Φ at a given wavelength λ is determined by the cavity length D through $\Phi=2\pi D/\lambda$ and $F=1.04$ is the measured cavity contrast.

More details on the analysis of the optical resonator and its applications to the interferometric Rayleigh scattering of single QDs can be found elsewhere.[5,6] Here, we highlight the fact that the transmitted and reflected intensity oscillate when the coherence length of the light exceeds the cavity length. An example is shown in Fig. 3(b). The reflected power is a smooth function of the vertical translation through the focal plane in the case of incoherent illumination (diode laser operated below the threshold), whereas intensity oscillations with a period of $\lambda/2$ are observed if the illumination at the same wavelength λ is coherent (above threshold laser operation). It should be noticed that the optical Fabry–Pérot cavity is not an unavoidable but an additional feature of the micro-
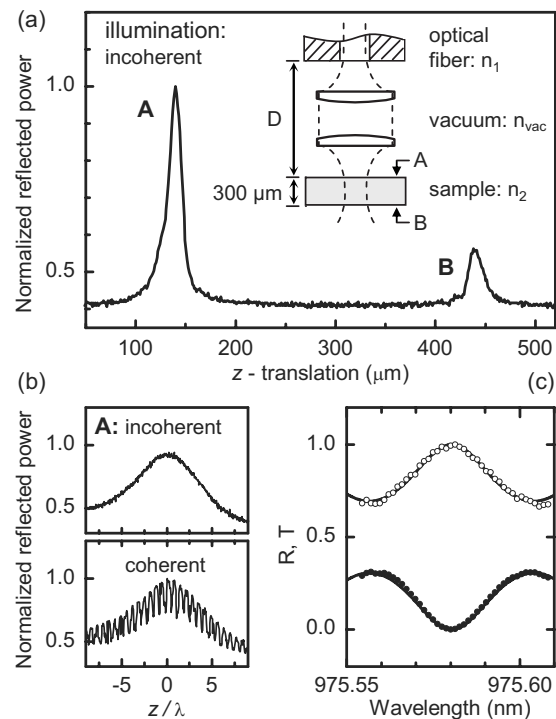
FIG. 3. (a) Normalized reflected power as a function of axial (z) translation of the sample under incoherent illumination at 950 nm wavelength. Strong (A) and weak (B) resonances resulting from reflection from the sample interfaces are observed as the sample is moved upwards through the focal plane of the microscope. The inset shows the schematics of the confocal Fabry–Pérot resonator of length D formed by the polished fiber end and the sample surface with refractive indices n_1 and n_2, respectively. (b) Resonance peak A for coherent (top) and incoherent (bottom) illumination. The z-translation is normalized to the illumination wavelength. (c) Normalized transmission (open circles) and reflectivity (solid circles) of the arrangement sketched in (a) plotted against illumination wavelength together with fits to the Fabry–Pérot functions (solid lines).

scope concept. The resonator finesse can be controlled by adjusting the optical interfaces. Control of the sample-vacuum reflectivity is potentially complicated. Regarding the fiber-vacuum interface, however, the reflectivity of the fiber end can be improved yielding a higher contrast, for example, by deposition of a metallic or a dielectric distributed Bragg reflector, or conversely, the cavity effect can be strongly suppressed with an antireflection coating or by angle cleaving the fiber for minimum back reflection (reflectivity less than 10^{-4}).

B. Resolution

The spatial resolution of the microscope was determined at 4.2 K at the illumination wavelength of 950 nm by imaging an aluminum grating on quartz. The aluminum features are defined with sub-100 nm precision by e-beam writing. An image of a 10 μm period aluminum grating taken with a commercial microscope is shown in the inset of Fig. 4. When the grating was positioned in the focal plane, the transmitted signal revealed oscillations in intensity as a function of the transverse x-coordinate, upper panel of Fig. 4. The transmission through the grating is given by a convolution of the Gaussian focal intensity distribution with the transmission function of the grating. Since the edges of the highly reflect-
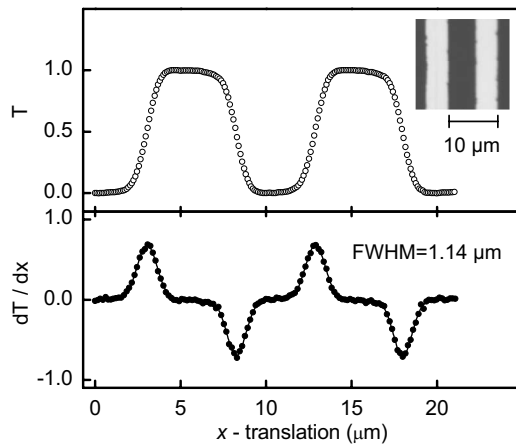
FIG. 4. Determination of the optical resolution. Upper panel: normalized transmission (open circles) of the alignment laser (wavelength of 950 nm) through an aluminum grating with a period of 10 μm as a function of the x-translation. The inset shows a micrograph of the grating recorded with a commercial microscope in reflection mode, bright stripes correspond to the highly reflective aluminum, and dark stripes result from the low reflective quartz plate. Lower panel: numerical derivative of the normalized transmission trace (circles) and the corresponding fit with four convolved Gaussians (solid line). The resolution corresponds to the averaged full width at half maximum FWHM$=1.14\pm0.2$ μm.

ing aluminum stripes are sharp on the scale of the focal spot diameter, the grating transmission can be approximated by a step function.

The resulting characteristics of the transmitted power T are determined by the Gaussian error function, exactly as measured (Fig. 4, upper panel). The corresponding derivative dT/dx is shown in the lower panel of Fig. 4. Best fit to the derivative is obtained with four Gaussian functions (black solid line), one for each edge. We find an averaged experimental resolution of full width at half maximum (FWHM) $=1.14\pm0.2$ μm. In another realization of the microscope, we measured a FWHM of 0.9 ± 0.1 μm. These results are in agreement with the resolution expected from diffraction. Focusing a plane wave results in FWHM$=0.52\lambda/$NA $\simeq 0.89$ μm for 950 nm illumination wavelength. In our case, the illumination is a truncated Gaussian beam (consistent with the absence of Airy rings in Fig. 4) and this increases the FHWM slightly to 0.98 μm, as calculated following Ref. 7.

In reflection mode, the light passes through the microscope twice, the origin of the confocal enhancement to the resolution. Consistent with this, we find a smaller resolution in reflectivity with a typical FWHM of ~ 1 μm. To monitor the chromatic aberration, we focused the microscope using a 950 nm laser diode and then without further adjustments, we measured the resolution using a 850 nm laser diode. We find that the FWHM increases to 1.6 ± 0.1 μm. The chromatic aberration is therefore not severe in this case. We stress that the diffraction limit can also be achieved for 850 illumination, but not for 850 nm and 950 nm simultaneously.

C. Imaging

An example of the imaging performance of the optical system is presented in Figs. 5 and 6. The confocal image in Fig. 5 was recorded in reflection with the microscope cooled
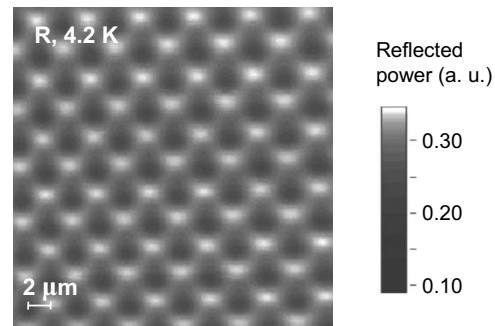

FIG. 5. Confocal image of a chessboard sample (SiO$_2$ on Si, 1×1 μm^2 with 2 μm period) recorded in slip-stick step-scanning reflection mode at 633 nm illumination. The total scanned area is about 12×12 μm^2, the step size was 50 nm, and the temperature 4.2 K.

to 4.2 K. The object is a regular arrangement of silicon oxide (SiO$_2$) squares on silicon (Si) of size 1×1 μm^2 and a 2 μm period. Different amplitude reflectance coefficients of Si and SiO$_2$ result in a modulation of the reflected power. The confocal image was acquired with incoherent illumination pixel by pixel as the x- and y-positioners were moved stepwise with a step size of 50 nm. The image is extraordinary regular without significant distortion or hysteresis and reflects the regular "chessboard" pattern. We note that no adjustment of the z-position was necessary in order to maintain the homogeneous contrast throughout the scanning range, despite the fact that the reflected power is a sensitive function of axial displacement (as seen in Fig. 3). This indicates that for a nontilted sample as in our case the displacement cross-talk between the positioning axes is negligible. Further details of the slip-stick scanning regime are discussed elsewhere.[8]

As an alternative, image acquisition can be achieved in continuous scanning mode. At room temperature, a dc-voltage ramp from 0 to 150 V applied to the piezoelectric rods of the positioners provides displacement up to ~ 4.5 μm on each axis. The scanning range is reduced by a factor of 3 at 77 K and a factor of 10 at 4.2 K.[9] However, the voltage range can be extended at low temperatures without any damage to the piezo rods such that voltages from -300 to 300 V can be used at 4.2 K. Images of the chessboard pattern recorded under ambient conditions are presented in Fig. 6. The optical reflectivity signal is shown in the left graph, while the transmission photosignal in the right. Both signals were detected simultaneously, and there is a clear complementary
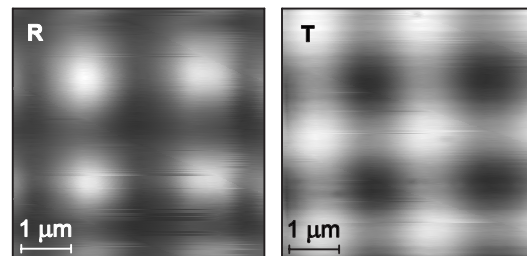

FIG. 6. Images of the chessboard sample shown in Fig. 5. The images were recorded in continuous x-scanning mode in reflection (left) and transmission (right) at 950 nm wavelength illumination. The total scanned area is about 4.5×4.5 μm^2 in both images. The displacement was controlled with a dc voltage ramp (0–150 V at 300 K) applied to the piezoelectric components of the positioners.
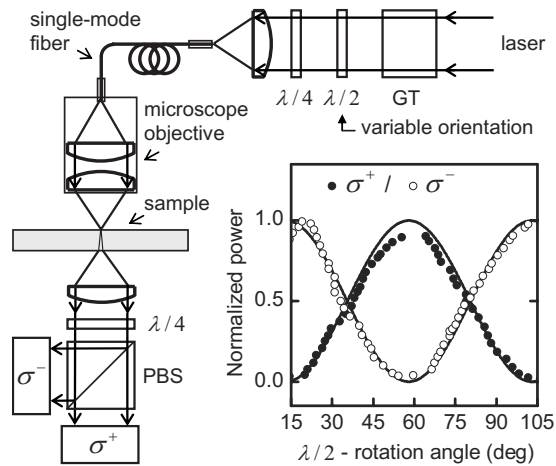
FIG. 7. Schematics: setup for polarization control in transmission. The linear polarization of the laser is defined with a Glan–Thompson polarizer. The incident angle of the polarization axis with respect to the quarter waveplate $\lambda/4$ is varied with the $\lambda/2$ waveplate before coupling into the single-mode microscope fiber and focused onto the sample. The transmitted light is collimated and analyzed with a combination of another quarter waveplate $\lambda/4$ and a polarizing beam splitter on the two photodetectors labeled with σ^- (left-handed circular) and σ^+ (right-handed circular). The compact polarization analysis unit was located in the microscope assembly below the sample and could be used under both ambient and cryogenic conditions. The graph depicts a room-temperature measurement of the normalized detector powers (circles) as a function of rotation angle defined by the half waveplate.

response in the photosignals R and T to the reflecting and transmitting regions, as expected. The high-quality imaging results of Figs. 5 and 6 confirm the functionality of the present microscope.

D. Polarization

One of the major concerns associated with the use of glass fibers is the effect of the fiber on the light polarization. In many cases, polarization information is lost on the way through the fiber due to birefringence induced by uncontrolled fiber bending. However, for a given fiber arrangement, the output polarization state is a constant function of the input polarization state. Furthermore, the contribution of the fiber to the polarization can be compensated by adjusting the input polarization allowing the creation of arbitrary polarization states at the fiber output. In order to probe these effects in our microscope, a test experiment was performed where the state of the light polarization was analyzed below the sample with a setup illustrated in Fig. 7.

The laser polarization was defined by a Glan–Thompson linear polarizer and a combination of half and quarter waveplates before the input to the microscope fiber. The light transmitted through the sample was collimated and analyzed with a quarter waveplate and a polarizing beam splitter. Two photodiodes then analyze the polarization state by detecting the right-handed circular (σ^+) and left-handed circular (σ^-) polarization states (the propagation direction is antiparallel to the z axis). The graph in Fig. 7 demonstrates that an arbitrary elliptical polarization state can be defined at the sample. In particular, pure left-handed or right-handed circular polarization can be defined[10] by rotating the half waveplate to an appropriate orientation. This experiment was performed at 300 as well as at 77 and 4.2 K without significant change in
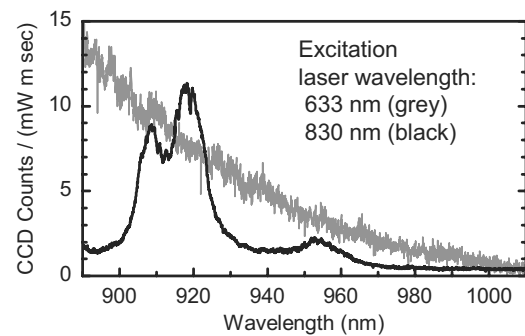

FIG. 8. Fiber related background in the relevant spectral range of the quantum dot luminescence of 900–1000 nm normalized to the excitation power, fiber length, and integration time. In contrast to the monotonic decay for the excitation with a He–Ne laser (633 nm), the fiber background signal for the 830 nm excitation shows distinct peaks.

polarization characteristics and demonstrates that full control over the polarization state at the sample is possible with the fiber-based microscope. Potentially, the reflected light could be used for an *in situ* analysis of the polarization state without the need for analyzing polarization optics at 4.2 K. However, the Faraday effect on the polarizing properties of the glass fiber can be significant in high magnetic fields and should be kept in mind. For applications where circular polarization must be maintained, the effect of the magnetic field induced Faraday rotation of the polarization axis is irrelevant since it affects both in-plane polarization components equally but does not alter the phase shift between them.

E. Fiber-related background

For some applications, the use of the fiber as an optical guide can have the disadvantage of fiber associated background fluorescence and Raman scattering. In the case of our experiments performed on QDs, however, the fiber related background signal can be neglected in PL spectroscopy application and is completely irrelevant for the resonant transmission spectroscopy. In order to quantify the undesired background, we investigated its dependence on the fiber length as well as on the power and wavelength of the excitation laser. The result for the fiber-related background in the relevant spectral range of InGaAs QD PL is shown in Fig. 8. The spectral intensity distribution is different for the two excitation wavelengths of 633 and 830 nm. Excitation at 830 nm caused distinct resonances in the fiber spectrum, whereas the response to the He–Ne excitation decayed monotonically while still having the same order of magnitude in intensity. The origin, polarization, and direction of the fiber background have not been investigated in detail. The Raman scattering induced in the fiber is expected to be spectrally localized around the excitation wavelength and is therefore unimportant for nonresonant excitation of QD PL. The fiber fluorescence is more troubling. An upper limit for the fiber contribution in our QD PL experiments can be given. Typically, a laser diode operating at 830 nm wavelength below 100 μW input power was used for the PL excitation. Given a microscope fiber length of ∼2 m, the maximum resulting fiber contribution is ∼2 counts/(s pixel), at least an order of magnitude lower than the characteristic QD
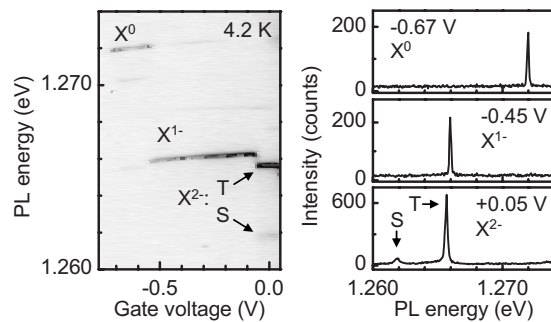
FIG. 9. Photoluminescence from a single InGaAs quantum dot at 4.2 K. Left panel: gray scale charging diagram shows the emission energy dependence on the voltage applied to the gate electrode of the sample (black and gray colors represent high and low emission intensities, respectively). Plateaus of constant intensity are labeled with X^0, X^{1-}, and X^{2-} for the neutral, singly charged, and doubly charged exciton recombinations. The triplet (T) and singlet (S) emission resonances of the doubly charged exciton are denoted with arrows. Right panel: single spectra of the neutral and charged exciton transitions at the corresponding gate voltages. The spectral resolution is limited by the spectrometer to 150 μeV.

PL response leading to high signal-to-noise ratio. In fact, the constant fiber signal can be removed from the spectra by background subtraction.

IV. APPLICATION TO QUANTUM DOT SPECTROSCOPY

In order to exemplify the high performance of the microscope, we present in the following PL and magneto-PL data of single self-assembled QDs.

The QDs used in our spectroscopy experiments are based on InAs and GaAs compound semiconducting materials and were grown by molecular beam epitaxy in a self-assembly growth mode.[11,12] The nanometer sized islands trap optically excited electron-hole pairs, the so-called excitons, within the local potential minima of the conduction and valence bands. The emission of the QD originates from the radiative recombination of the localized excitons and is centered at 940 nm wavelength (emission energy of 1.32 eV). Typically, a laser wavelength above the band gap of GaAs (~820 nm), the embedding semiconductor matrix material, is chosen for carrier pair excitation. Given the chromatic aberration of the microscope, positioning of the sample is performed with an alignment laser at 950 nm wavelength prior to switching the fiber beam splitter to the excitation laser (see Fig. 1). The PL signal is directed with the signal arm of the beam splitter to the monochromator with a nitrogen-cooled charge coupled device (CCD).

Figure 9 shows PL originating from a single charge-tunable self-assembled InGaAs QD. PL characteristics of single charge-tunable quantum rings were reported previously;[13] here, the data were obtained from a similar sample. The QDs are embedded in a field-effect structure which allows for single electron charging of the QDs by exploiting a tunneling interaction between the dots and an electron reservoir.[13,14] The charging signature is represented in a characteristic gray scale plot in the left panel of Fig. 9. Pronounced Coulomb blockade plateaus of nearly constant PL emission energy as a function of gate voltage are the significant features in the charging diagram. The plateaus are
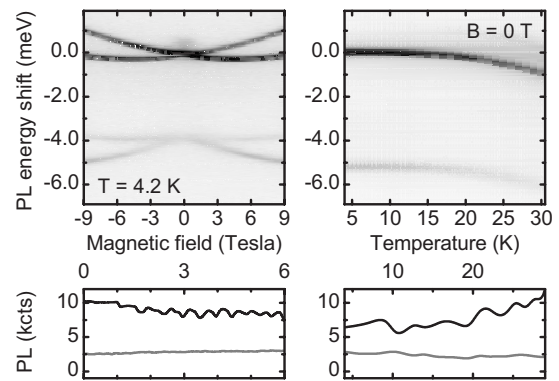

FIG. 10. Energy dispersion (upper panel) of the excitonic triplet and singlet recombination lines as a function of magnetic field (left) and temperature (right). Intensity oscillations (lower panel) visible in the triplet (black solid lines) luminescence are attributed to a Fabry–Pérot resonator effect. In contrast, the coherence length of the singlet emission is not sufficient to cause significant modulation of the emission intensity (gray solid lines) by interference in the optical cavity.

labeled with X^0, X^{1-}, and X^{2-}, denoting the radiative recombination of the neutral, singly, and doubly charged excitons, respectively.

Emission spectra originating from the recombination of single X^0, X^{1-}, and X^{2-} transitions at gate voltages of −0.67, −0.45, and 0.05 V, respectively, are shown in the right panel of Fig. 9. The X^{2-} recombination is split because of an electron exchange interaction in the final state of the recombination process. There are two final states, the triplet, and singlet, resulting in two recombination lines, labeled as T and S and denoted with arrows. The energy splitting of the S and T PL lines is equal to twice the exchange splitting involving an *s*-shell electron and a *p*-shell electron. It is relatively large as a consequence of the strong confinement. The linewidth of the triplet state is limited by the resolution of our spectrometer to 150 μeV and does not reflect the natural linewidth. The linewidth of the singlet is well resolved; it is ~600 μeV.

The evolution of the emission energy of the doubly charged exciton lines with magnetic field and temperature is presented in Fig. 10. The magnetic field dispersion of the X^{2-} is displayed in a gray scale plot in the left panel. The field splits both the triplet and the singlet lines into two branches through the Zeeman effect. The Zeeman splitting increases linearly with magnetic field; there is also a parabolic dependency of the energy positions arising from the diamagnetic shift.[15,16] The significant point from an instrumental point of view is that no adjustment was necessary during the sweep of the magnetic field in the interval of −9−+9 T; the exciton PL remains strong and clearly distinguishable from the background, even in the case of the weak singlet line. This is a clear demonstration of the spectacular stability of the microscope system against large magnetic field gradients.

The temperature sweep in the right panel of Fig. 10 was obtained in a different measurement cycle on another QD. The temperature was controlled locally on the sample holder with a dissipative high-resistance heater and monitored with an on-site sensor. Again, within the full range of the sweep up to 30 K, realignment of the system was not required. The evolution of the singlet and triplet PL lines is clearly visible, a detailed analysis can be found elsewhere.[17] From the qual-

ity of the data in Fig. 10, the high mechanical stability of the microscope against thermal gradients is obvious.

An interesting feature of the PL measurements is that weak intensity oscillations arise as the magnetic field and temperature are scanned (Fig. 10). The PL intensity oscillation is evidenced in the case of the triplet emission but absent in the singlet emission in both graphs of Fig. 10. The oscillatory intensity fluctuations are attributed to the transmission characteristic of the Fabry–Pérot optical resonator described earlier. Due to the shift of the emission wavelength caused by the magnetic field or temperature, the PL is modulated in the same way as the transmitted power of the alignment laser in Figs. 3(b) and 3(c). Thus, the coherence length of the triplet emission must exceed the cavity length D. The upper limit of the corresponding excitonic linewidth is 20 μeV which is too small to be resolved with out spectrometer. The coherence length of the singlet line, however, is far below the limit required for the interference effects to appear. From the spectral linewidth of 600 μeV, we can deduce a coherence length of 0.3 mm, 30 times smaller than the cavity length. For this reason, as in Figs. 3(a) and 3(b) for incoherent illumination, oscillations of intensity with wavelength should not be present in the singlet PL, exactly as we observe in Fig. 10 and consistent with the cavity analysis given in the preceding section. This example shows how the microscope's intrinsic interferometer can be exploited profitably.

Further evidence for the extraordinary mechanical stability of the microscope setup is the fact that helium refilling of the cryostat had no influence on the sample position. In order to maintain the temperature at 4.2 K, the bath cryostat was repeatedly refilled every ∼40 h in measurement runs ongoing for several weeks. This has allowed us to investigate the same QD for more than 2 months without adjustments to the alignment before data acquisition was completed and the system was warmed up to ambient conditions. We believe that this feature will be very important in the future as single quantum dot experiments become more sophisticated.

V. SUMMARY

The realization of a new concept of confocal microscope for cryogenic spectroscopy is presented. The microscope system is very compact and therefore allows for adjacent positioning of the sample and objective in a common monolithic titanium housing. As a consequence, the relative alignment of the sample and microscope objective is not influenced by thermal or magnetic gradients allowing for high-stability spectroscopy at liquid helium temperatures. Low-temperature compatible piezobased positioners provide the capability of sample scanning with nanometer precision in all three directions over a range of approximately millimeters. The microscope is coupled to the external world via a single-mode optical fiber. As a demonstration of the high performance of the microscope, applications in low temperature spectroscopy of single quantum dots is presented. Our microscope concept holds great promise for optical spectroscopy at ultra low temperatures. All the components are compatible with millikelvin temperatures accessible with dilution refrigerators or adiabatic demagnetization refrigerators. The construction of an ultra low temperature system is presently in progress.

[1] S. Kimura and T. Wilson, Appl. Opt. **30**, 2143 (1991).

[2] *Confocal Microscopy* edited by T. Wilson (Academic, London, 1990).

[3] D. W. Pohl, Rev. Sci. Instrum. **58**, 54 (1987).

[4] C. Renner, P. Niedermann, A. D. Kent, and O. Fischer, Rev. Sci. Instrum. **61**, 965 (1990).

[5] A. Högele, "Laser spectroscopy of single charge-tunable quantum dots," Ph.D. thesis Ludwig-Maximilians-Universität München, 2006.

[6] B. Alén, A. Högele, M. Kroner, S. Seidl, K. Karrai, R. J. Warburton, A. Badolato, G. Medeiros-Ribeiro, and P. M. Petroff, Appl. Phys. Lett. **89**, 123124 (2006).

[7] L. D. Dickson, Appl. Opt. **9**, 1855 (1970).

[8] C. Meyer, O. Sqalli, H. Lorentz, and K. Karrai, Rev. Sci. Instrum. **76**, 063706 (2005).

[9] M. Shayegan, K. Karrai, Y. P. Shkolnikov, K. Vakili, E. P. De Poortere, and S. Manus, Appl. Phys. Lett. **83**, 5235 (2003).

[10] A. Högele, S. Seidl, M. Kroner, K. Karrai, R. J. Warburton, M. Atatüre, J. Dreiser, A. Imamoğlu, B. D. Gerardot, and P. M. Petroff, J. Supercond. **18**, 245 (2005).

[11] D. Leonard, K. Pond, and P. M. Petroff, Phys. Rev. B **50**, 11687 (1994).

[12] J. M. Garcia, G. Medeiros-Ribeiro, K. Schmidt, T. Ngo, J. L. Feng, A. Lorke, J. P. Kotthaus, and P. M. Petroff, Appl. Phys. Lett. **71**, 2014 (1997).

[13] R. J. Warburton, C. Schäflein, D. Haft, F. Bickel, A. Lorke, K. Karrai, J. M. Garcia, W. Schoenfeld, and P. M. Petroff, Nature (London) **405**, 926 (2000).

[14] H. Drexler, D. Leonard, W. Hansen, J. P. Kotthaus, and P. M. Petroff, Phys. Rev. Lett. **73**, 2252 (1994).

[15] C. Schulhauser, D. Haft, R. J. Warburton, K. Karrai, A. O. Govorov, A. V. Kalameitsev, A. Chaplik, W. Schoenfeld, J. M. Garcia, and P. M. Petroff, Phys. Rev. B **66**, 193303 (2002).

[16] K. Karrai, R. J. Warburton, C. Schulhauser, A. Högele, B. Urbaszek, E. J. McGhee, A. O. Govorov, J. M. Garcia, B. D. Gerardot, and P. M. Petroff, Nature (London) **427**, 135 (2004).

[17] B. Urbaszek, E. J. McGhee, M. Krüger, R. J. Warburton, K. Karrai, T. Amand, B. D. Gerardot, P. M. Petroff, and J. M. Garcia, Phys. Rev. B **69**, 035304 (2004).